Article

A Photonically-Excited Leaky-Wave Antenna Array at E-Band for 1-D Beam Steering

Álvaro J. Pascual-Gracia [1], **Muhsin Ali** [2], **Guillermo Carpintero Del Barrio** [2], **Fabien Ferrero** [3], **Laurent Brochier** [3], **Ronan Sauleau** [1], **Luis Enrique García-Muñoz** [2,*] **and David González-Ovejero** [1,*]

1   Univ Rennes, CNRS, IETR (Institut d'Electronique et de Télécommunications de Rennes)–UMR 6164, F-35000 Rennes, France; alvaro-jose.pascual@univ-rennes1.fr (Á.J.P.-G.); ronan.sauleau@univ-rennes1.fr (R.S.)
2   Universidad Carlos III de Madrid, 28911 Leganés, Spain; muali@ing.uc3m.es (M.A.); guiller@ing.uc3m.es (G.C.D.B.)
3   Université Côte d'Azur, CNRS, LEAT (Laboratory of Electronics Antennas and Telecommunications)–UMR 7248, 06903 Sophia Antipolis, France; fabien.ferrero@unice.fr (F.F.); laurent.brochier@unice.fr (L.B.)
*   Correspondence: legarcia@ing.uc3m.es (L.E.G.-M.); david.gonzalez-ovejero@univ-rennes1.fr (D.G.-O.)

check for updates

Abstract: This manuscript reports the first leaky-wave antenna (LWA) array excited by a photomixer as well as its potential application for alignment in wireless links. The designed array is manufactured in printed circuit board (PCB) technology, works at the E-band (from 75 to 85 GHz), and provides a directive beam of about 18 dBi with a frequency scanning span of 22°. The antenna element consists of a microstrip line periodically loaded with stubs, and it has been designed employing a hybrid approach combining full-wave simulations and transmission line theory. This approach enables the optimization of the periods when the open-stopband of the LWA is mitigated or removed at the frequency of broadside emission. The proposed antenna was first tested using a ground signal ground (GSG) probe; the measured return loss and radiation patterns of the fabricated prototype were in good agreement with full-wave simulations. Then, the LWA array was integrated with the photomixer chip using conductive epoxy threads. Measurements of the radiated power yielded a maximum of 120 μW at 80.5 GHz for a 9.8 mA photocurrent. Finally, the antenna was used in a 25 cm wireless link, obtaining a 2.15 Gbps error-free data rate.

Keywords: photomixer; photonic antenna; PCB antenna; E-band; beam scanning; beam steering; probe de-embedding; leaky-wave antenna; epoxy bonding; RF choke

1. Introduction

Photonic generation of millimeter (mm) and submillimeter (sub-mm) continuous-wave radiation by photomixing is an extremely promising route to explore. In this approach, two optical wavelengths are mixed on a fast photodetector, such as a uni-traveling carrier photodiode (UTC-PD). The electrical beat note at the output of the photodetector is equal to the frequency difference of the two optical tones. Photomixing is advantageous to electronic generation in terms of coherence length and bandwidth of the generated carriers [1]. Moreover, one can use reliable and cost-effective optical components such as Erbium-doped fiber amplifiers (EDFAs), semiconductor optical amplifiers (SOAs), switches or time delay lines. Besides, due to the seamless integration with fiber optics, photonically-excited antennas are commonly used in wireless links at terahertz (THz) and sub-THz frequencies with multi-Gbps data throughput [2–5]. The main downside of photonic generation is the relatively low output power. Photonic transmitters typically use substrate lens antennas [6], horns [7], horns as feeds of quasi-optical

(QO) systems [8,9], and, less commonly, alternative antenna topologies such as tapered slot antennas [3] or monolithically integrated transverse electromagnetic horns [10]. In general, these antennas present a challenging escalation [11,12].

The difficulty of integrating several photomixer-excited antennas has obstructed the development of arrays with beam steering capabilities, and just a few demonstrations can be found in the open literature [13,14]. Beam steering would extend the range of applications of this kind of antennas. Among possible use cases, to name a few, one can find imaging systems, fine beam alignment to compensate mast misalignment or twist and sways from mounting structures [15], or reconfigurable wireless links in data centers [16].

The development of photomixer-excited antennas with beam steering could unlock the use of the E-band (71–76 GHz, 81–86 GHz), which presents several advantages. It offers a 2×5 GHz bandwidth, adequate for tens of Gbps of data transmission; it does not present the absorption peak of oxygen compared to the 60–GHz band, and the free-space loss is lower than at higher sub-mm wave frequencies.

The availability of low-loss, thin, inexpensive substrates well adapted to this frequency range makes printed circuit board (PCB) technology a promising approach for the realization of photonic transmitters/receivers (Tx/Rx). Active components with complex polarization networks can be integrated with passive components in a single multilayered board, as in [17]. Furthermore, in [3,18] we demonstrated the possibility of developing a photonic Tx with this technology.

This work presents, to the best of our knowledge, the first realization of a leaky-wave antenna (LWA) excited by a photomixer, as a simple means to steer the beam with frequency in 1-D. The LWA is printed using PCB technology and works at the upper window of the E-band. It would find applications in some of the cases cited above. In particular, the case where the proposed antenna is used for automatic alignment in line-of-sight (LoS) mm-wave links will be discussed in more detail here. The realized design features a fairly broad relative bandwidth (>10%), and allows a scanning range of 22°, including broadside. Moreover, the scalability of the presented layout is beneficial with respect to classical mm-wave antennas to combine several emitters and increase emitted power and or directivity.

Section 2 describes the design of the antenna. The integration of the photodiode chip with the PCB is discussed in Section 3. Sections 4 and 5 present measurement results and a potential application, respectively. Finally, conclusions are presented in Section 6.

2. Leaky-Wave Antenna

This design is motivated by the necessity of increasing the emitted power by a scalable layout, with beam steering capabilities, and a 10% relative bandwidth around the center frequency (81 GHz). One of the simplest beam steering methods is frequency steering with a 1-D periodic LWA. In this configuration, a traveling wave encounters periodic perturbations in one direction, so that it leaks progressively. If the electrical path between successive perturbations is such that the traveling wave encounters them in phase, the antenna will radiate a beam at or near broadside, as is clear from the array factor. Conversely, as frequency increases, the electrical path between elements will also increase, and the array factor will produce a beam moving from the backward to the forward quadrant [19].

Figure 1 shows a top view of the proposed antenna, its different parts, and the unit-cell of the radiating section, all described in detail hereinafter. The geometrical features were printed on a grounded Duroid 5880 substrate ($\varepsilon_r = 2.24$, $\tan\delta = 0.004$ at 60 GHz), suitable for high-frequency applications. At mm-wave frequencies, these values are a more exact determination of the relative permittivity than the typical values used ($\varepsilon_r = 2.20$, $\tan\delta = 0.0009$ at 10 GHz) [20]. The chosen thickness is the minimum among the standards (127 μm) to minimize the radiation losses and the power lost to surface-waves [21] of the different printed structures. The antenna is excited by a 2×1 array of UTC-PD on InP. Each UTC-PD presents a 50-Ω grounded coplanar waveguide (G-CPW) output and feeds two rows of the array. The length of each row is truncated by a matched patch, where a longer row will

feature a more directive beam. Additionally, this design is scalable in the direction perpendicular to the rows, so that more rows can be added. By controlling the number of rows and their length, one can easily accomplish symmetrical patterns (at E- and H-planes) or increase the directivity or the emitted power. In this respect, the proposed structure is advantageous to other classical sub-millimeter wave antennas, such as horns or on-chip antennas with silicon substrate lenses, which are more challenging to escalate. The antenna was designed using a full-wave simulator (ANSYS HFSS, version 19.0.0) and transmission line modeling for fast and preliminary layouts.
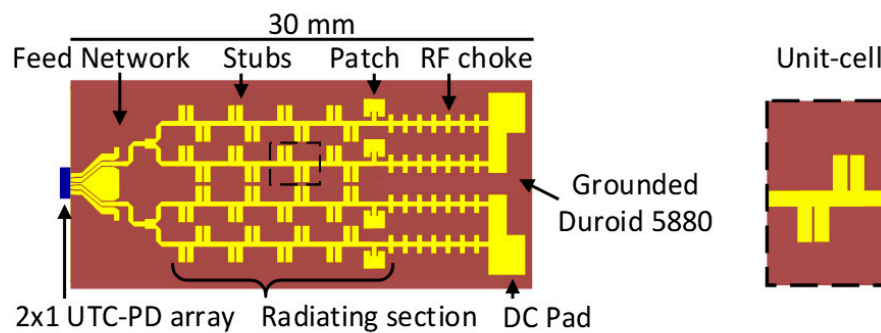

Figure 1. Layout of the designed antenna with the different sections indicated, and unit-cell of the radiating section.

2.1. Feed Network

The antenna feed network comprises the section between the photodiode chip and the rows. It is composed of a tapered transition to adapt the width difference between the photodiode output and the 50-Ω G-CPW on the Duroid 5880 substrate (as detailed in Figure 6a). After this transition, a section follows in which the two G-CPWs separate to conform to the row separation. Finally, the last section is a transition to a microstrip transmission line (TL) and a symmetric corporate feed network for the array rows. It was designed to minimize the reflection coefficient, cross-talk between photodiodes, and the radiation losses that could degrade the patterns.

2.2. RF Choke

Antennas integrated with photodiodes often require a polarization network to enhance the photodiode responsivity. Therefore, one must include an RF choke at the end of each row to separate the radiating section from the pads used to polarize the UTC-PD. The choke is developed in microstrip technology, and it features a simulated RF isolation better than 35 dB within the array operating frequency band. It consists of seven cascaded identical sections, as shown in Figure 2 (right). Each section is T-shaped, and the horizontal bar is composed of two parallel, λ/4 open-ended stubs. The stubs create a short-circuit, resulting in an RF choke. Besides, the length of the T's vertical bar is chosen to translate the shorted microstrip to a large inductive load, so that it presents high input impedance, and this effect is reinforced, cascading them. Figure 2 (left and center) represents simulated and calculated isolation, $|S_{21}|$, depending on the number of sections as well as the magnitude of the reflection coefficient, $|S_{11}|$, for the 7-section choke, which is better than –0.85 dB in the whole band. In practice, the stubs do not create an exact short-circuit, and several sections need to be cascaded. Calculations are performed retrieving the ABCD matrix of the parallel stubs from full-wave simulations, taking the vertical bar as a section of a transmission line, and cascading the sections.
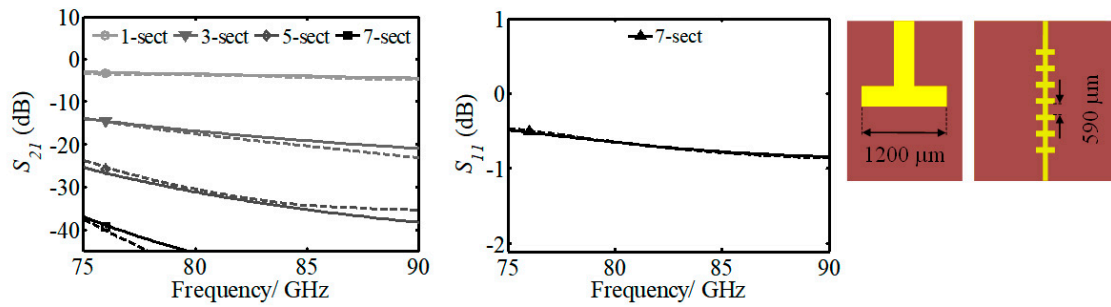
Figure 2. Left: Magnitude of isolation, $|S_{21}|$, for a choke composed of 1, 3, 5, and 7 sections. Center: magnitude of the reflection coefficient, $|S_{11}|$, for a 7-section choke. Continuous line: calculated by a transmission line (TL) equivalent. Dashed line: simulated. Right: View of the choke.

2.3. Radiating Section

The radiating section of the array comprises four identical rows. Every row consists of a microstrip line periodically loaded by groups of four stubs plus a patch that truncates it, as shown in Figure 1. The design of the periodic structure is crucial to obtain low values of $|S_{11}|$, as explained below.

One of the difficulties encountered while designing a 1-D periodic LWA is the scan through broadside. At this point, all reflections from the perturbations add in phase back to the source. This can create a bandgap in the *k-β* diagram; in this case the wave does not propagate into the structure and is completely reflected, degrading the input impedance matching. Following the discussion in [19], the perturbations of the periodic structure are modeled in a simplified network by shunt impedances connected by segments of TL. At broadside emission, the wave impinges the perturbations in phase, and the equivalent network is a shunt of infinite loads, which produces a short-circuit and the structure reflects the wave completely. On the other hand, if substantial losses are introduced by each perturbation, the current will progressively decay, effectively breaking the infinite periodicity, and a short-circuit will not be achieved. Hence, the latter case will present better matching characteristics.

In practice, each perturbation introduces losses and reflections to some degree. They have to be traded-off to obtain the desired radiation and impedance matching characteristics. Since the full-wave simulation of electrically large structures can be a computationally intensive task, it is preferable to use approximate criteria to optimize the period of the structure at the frequency of broadside radiation. To that end, it is assumed that coupling and surface-wave generation are negligible. In [22] it was shown that a spacing larger than $0.1\lambda_g$ leads to tolerable coupling effects between stubs in a loaded microscrip, where λ_g is the guided wavelength in the microstrip TL. The calculation consists of computing the *S*-parameters of an N-periods structure (S^{Tot}), from the scattering matrix of just one. The structure is assumed to be terminated in a matched load, and only the first bounce is considered for reflections, whereas for transmission no bounces are summed up. This is true only if $|S_{21}| >> |S_{11}|$. In this manner, the following calculation yields expressions that can be readily computed and used for optimization:

$$S_{11}^{Tot} \approx S_{11} \sum_{n=0}^{N-1} S_{21}^{2n} \tag{1}$$

$$S_{21}^{Tot} \approx S_{21}^{N} \tag{2}$$

The results from Equations (1) and (2), along with the exact computations, are shown in Figure 3 for a 10% and a 20% loss per pass ($|S_{21}| = \sqrt{0.9}$, $\sqrt{0.8}$, respectively). A symmetric unit-cell with $S_{11} = S_{22}$ was assumed to compute the exact values. $|S_{11}|$ is taken proportional to $|S_{21}|$ so that the infinite periodic structure presents S_{11}^{Tot} equal to –10 dB (and the bandgap can be considered effectively removed in terms of impedance matching). Figure 3 shows the largest deviation between exact and approximate curves. It occurs when the phase of S_{11} equals π. Second and higher-order even bounces add in phase with the traveling wave, yielding lower transmission losses than the approximate

calculation. Additionally, third and higher-order odd bounces add in phase with the first bounce so that S_{11} is underestimated in the approximate curves. As $\left| S_{11}^{Tot} \right|$ decreases, the agreement is better, while it degrades the other way around. In the latter case, the effects of stationary waves should be included computing multiple bounces. Finally, it is worth mentioning that as the losses per pass increase, $|S_{11}|$ can be proportionally larger that $|S_{21}|$ to achieve the same S_{11}^{Tot} threshold (the sum in Equation (1) approaches 1). Hence, increasing the losses per period relaxes the demand on S_{11} for adequate input impedance matching, in line with the earlier discussion. Note also that truncating the structure helps to decrease the reflection coefficient. Finally, for frequencies other than that of broadside directed emission, (1) and (2) can be adapted to introduce the phase change per period in S_{21}.
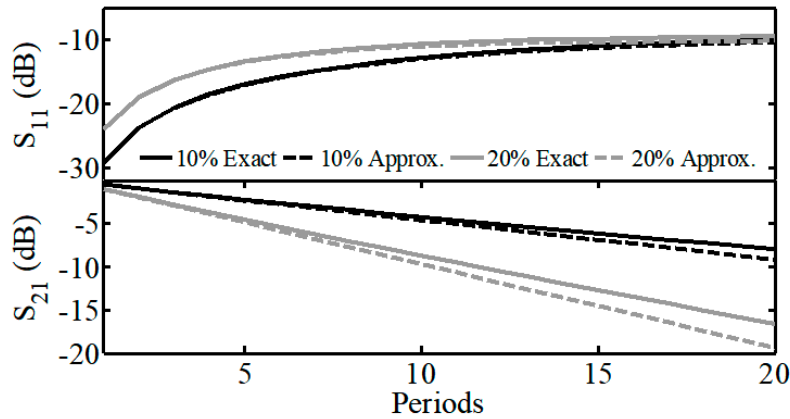

Figure 3. *S*-parameters as a function of the number of periods in the structure. Continuous line: exact calculation. Dashed line: approximate calculation from (1) and (2). The percentage indicates the power loss per pass of one period of the structure.

As an example of the usefulness of (1) and (2), we simulated the unit-cell reported in [23] (Figure 10) that removed the bandgap at broadside. The structure can be well described by a traveling wave, following our assumptions. S_{11}^{Tot}, S_{21}^{Tot} were computed for $N = 32$ and the approximate calculations yielded a return loss of 14.5 dB and a transmission loss of 16.3 dB, whereas simulation of the complete structure (using waveports at both ends) yielded 15.1 dB and 18.5 dB, respectively, with a CPU simulation time 18 times larger than the single unit-cell. This indicates that Equations (1) and (2) constitute a useful tool for preliminary optimization of this kind of structure.

The unit-cell used in our design was first reported in [22], and it is shown in Figure 4a. The stub length (*l*) is approximately λ/2, presenting high input impedance, to introduce a small perturbation in the TL, whereas its width (*w*) controls the amount of radiated power [22]. In turn, the stubs form groups of four: two towards the right and two towards the left, equispaced at distance *s*. This configuration allows one to increase the return loss if $\Delta arg(S_{21})$ per stub plus inner separation is approximately π/2. In addition, it introduces more losses per period, so that the design can be made more compact. On the other hand, the stubs do not radiate in phase but in quadrature. This results in a pattern that points off-broadside in the plane perpendicular to the row; this effect is conveniently eliminated by the array factor of the complete four-row structure. The simulated and calculated *S*-parameters using Equations (1) and (2) are shown in Figure 4b for broadside emission. The periodic structure presents $S_{11} < -12$ dB, and the calculated curve is in agreement with simulated values. The calculated values for S_{21} are slightly overestimated due to the excluding of the higher-order bounces in the calculation, as also occurred in Figure 3. Once the group of four stubs is optimized (Figure 4b), a segment of transmission line is added to obtain the required length, *p*, for a total phase change of 2π in S_{21} per period at the central frequency of operation. To do so, the *S*-matrix of the four stubs is retrieved from full-wave simulations, and the corresponding segment of TL is calculated. When several periods are simulated, the length of TL needs to be re-tuned. Its final value changes by about 4%. Hence, effects associated with surface waves and coupling introduce only a small perturbation. To show

the suppression of the open-stopband, Figure 4c represents the dispersion diagram and attenuation constant of the optimized unit-cell within the band of interest (solid black line). Dispersion and attenuation are also plotted for the same unit-cell geometry with $w = 50$ μm (solid grey line), and for a unit-cell with just a 50 μm wide stub (dashed grey line). In the latter cases, p is tuned to obtain $\Delta arg(S_{21})$ equaling 2π approximately at 81 GHz. For the unit-cell with one stub, note the typical open-stopband behavior around the frequency of broadside emission ($\beta_{-1}p/\pi = 0$) [19]. For $\beta_{-1}p/\pi$ equal exactly to 0, the wave is not radiated (α/k_0 equals 0), and it is totally reflected ($S_{11} > -1$ dB in the strop-band frequencies when a sufficiently large structure is simulated). For the four-stub unit-cell with $w = 50$ μm, the previous behavior is mitigated since the reflections from the stubs compensate to some degree, but it is still observed (in this case, $S_{11} = -3$ dB). Finally, for the designed unit-cell optimized using the approach explained before, the curves present a much smoother behavior, and the stopband effect is largely mitigated ($S_{11} < -12$ dB).
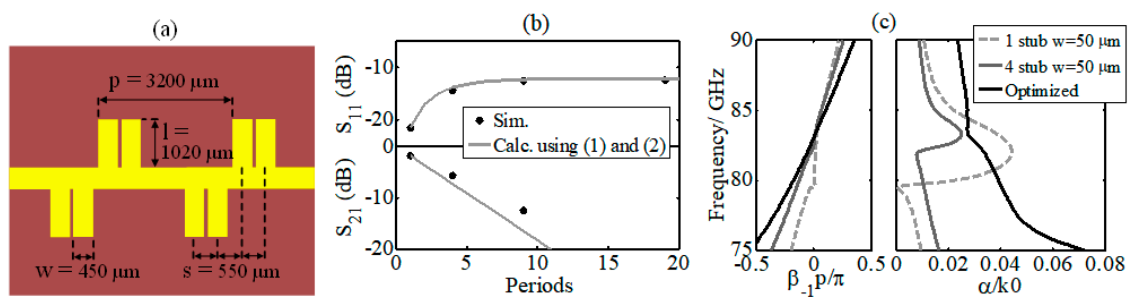

Figure 4. (**a**) Two consecutive periods along with representative geometrical parameters. (**b**) Optimized $|S_{11}|$ and $|S_{21}|$ for broadside emission as a function of the number of elements in the periodic structure (lines), and simulated values (dots). (**c**) Dispersion diagram and attenuation constant for three structures: the optimized one shown in (**a**) with 4 stubs per unit-cell and $w = 450$ μm (solid black lines), a 4-stub structure with $w = 50$ μm (solid grey lines), and a structure with a single stub per unit-cell with $w = 50$ μm (dashed grey lines).

Since the antenna will be tested in a wireless link with a QO parabolic mirror of 10.16 cm focal, its phase center should remain constant over the operation band. Therefore, a compact design (far-field at 10.5 cm), with broadside directed radiation (for simpler alignment) was targeted. For that purpose, the row is truncated after four periods in a patch that radiates the remaining power, between 10% and 25%. The resonance frequency of the patch is fixed to 85 GHz, slightly higher than the central frequency (81 GHz), to compensate for the lower losses at the higher end of the operation band. It is worth mentioning that the narrowband patch used to truncate the antenna and make it compact degrades the patterns beyond its resonance frequency, and thus, it limits the antenna bandwidth. In line with the application discussed in Section 5, by including more periods in the row, the bandwidth upper limit would be increased, the side-lobes would be decreased, and also it would help to obtain a narrower beam for more pointing resolution.

The above-described row is used to obtain the final planar array comprised of four rows. First, the row is duplicated to get a 2×1 array. Second, this 2×1 array is mirrored and excited in phase opposition, which leads to a significant reduction of the cross-polarization level and an E-plane pattern pointing at broadside. The final structure consists of an approximately square array with a simulated directivity between 18.5 and 20.0 dBi, side-lobe level (SLL) < -9 dB, a half power beam width (HPBW) $< 13°$, and a radiation efficiency better than 75% in the 75–86 GHz frequency range. Figure 5a shows the *S*-parameters of the whole structure, and Figure 5b depicts the E- and H-plane cuts at broadside (81 GHz). The UTC-PDs are simulated as 50-Ω lumped ports, which corresponds to the characteristic impedance of the output G-CPW of the photodiodes. In the future, one could envisage integration of the UTC-PD with a matching network, as in [24], whose output impedance is also 50 Ω.
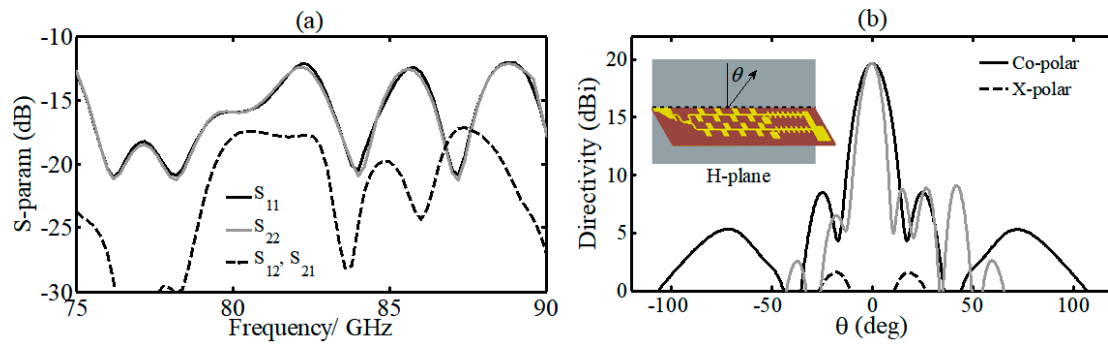
Figure 5. (**a**) Simulated magnitude of the reflection coefficient and cross-talk for the complete array. (**b**) Simulated E-plane (black) and H-plane (grey) cuts of the radiation pattern for broadside emission at 81 GHz.

3. Antenna and Photodiode Integration

In this section, we briefly describe the photodiode parameters and structure as well as its integration with the antenna. Additional details can be found in [3]. The available chip consists of two UTC-PD on InP. They are separated 500 μm, and each photodiode is integrated with a 50-Ω G-CPW (see Figure 6). The photodiode was reported in [25] and presents a 3 dB electrical bandwidth of 110 GHz. It is optically fed by a 4 μm spot-size lensed fiber as shown in Figure 6a,c. The measured UTC-PD responsivity is 0.17 mA/mW at 0 V bias.
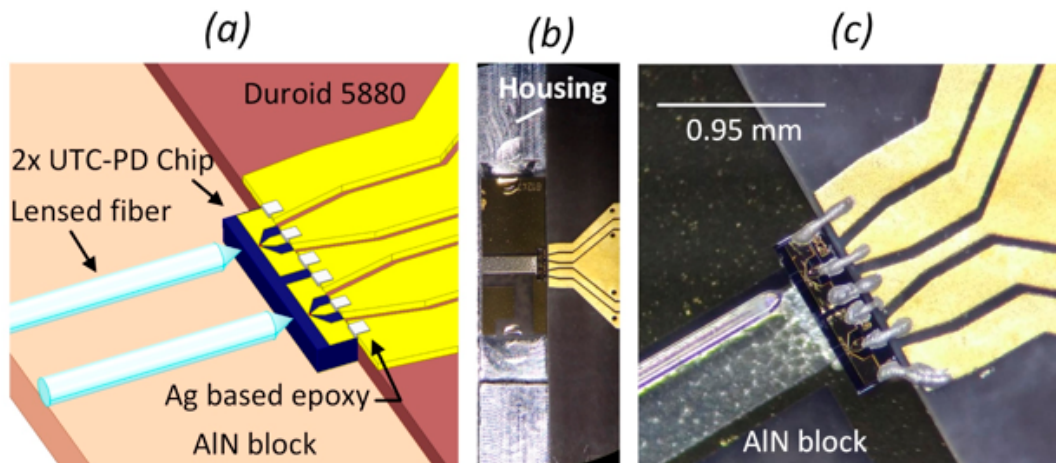

Figure 6. Images of the integration process: (**a**) designed transition, (**b**) AlN block and PCB aligned and glued to the housing, and (**c**) detail of thread bonding and fiber used to excite the UTC-PD.

The chip is mounted on an Aluminum Nitride (AlN) block for mechanical support, handling, and heat dissipation. During the integration process, the AlN block is positioned parallel to the PCB in such a way that the G-CPW of the chip is aligned and at the same height as the PCB (Figure 6b). Then, both are glued to a common housing, and the UTC-PD is finally bonded to the PCB using a silver-based conductive epoxy (Figure 6c). This approach results in a thick thread. Compared to wire bonding, it reduces the self-inductance of the wire, yielding a better electrical connection. This has been evaluated by bonding two sections of G-CPW on Duroid 5880 separated by 150 μm. The insertion losses (IL) obtained for ball wire bonding at 67 GHz are 1.4 dB higher than the IL using conductive epoxy.

4. Measurements and Results

Two different sets of measurements were carried out to evaluate the performance of the designed antenna: electronic measurements to determine return loss and radiation pattern, and photonic measurements to examine the power radiated and its performance in a wireless transmission link.

4.1. Electronic Measurements

The set of electronic measurements was performed on a two-row array prototype with a GSG probe (Form Factor ACP 110-T), and an Agilent N5242A vector network analyzer (VNA) with a mm-wave extension head (OML V10VNA2). The prototype included a tapered interconnection from the GSG pads to G-CPW to excite the antenna, as it can be seen in Appendix A Figure A2d,e.

For the reflection coefficient measurements, the procedure described in Appendix A was employed to de-embed the probe and interconnection. Measurement results are shown in Figure 7. The antenna was well adapted throughout the operation band and did not present an increased reflection coefficient at the frequency of broadside emission (81 GHz). The disagreement between simulation and measurement around 78 GHz could be attributed to an inexact value of the relative permittivity of the substrate used in the simulation, and to errors associated with the electrical connection between the probe and the PCB. Finally, tolerances in the fabrication of the PCB could also have impacted the performance. More precisely, VIA holes were positioned with an accuracy of $\pm$ 25 μm, which is comparable to the VIA-center to edge distance (150 μm).
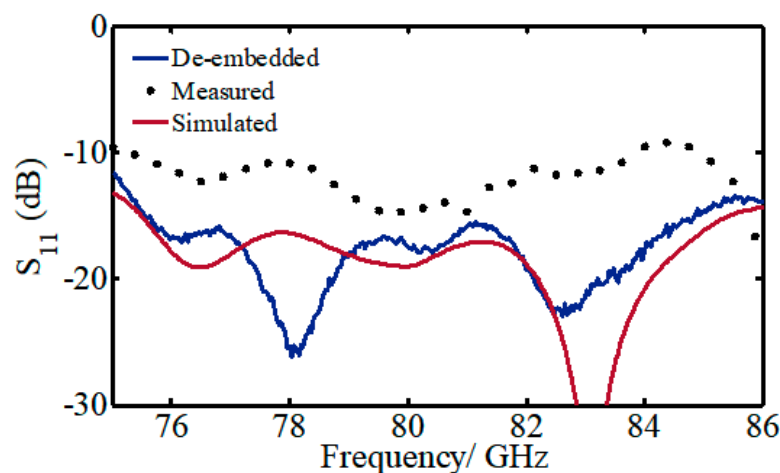

Figure 7. Magnitude of the reflection coefficient for the two-row prototype adapted for probe measurements. The black dots represent the measurement taken directly from the VNA, whereas the blue curve represents the measurement after de-embedding the probe and the interconnection.

For pattern measurements, a spherical 3D scanner and a receiving horn were additionally used. Figure 8a shows the normalized co-polar directivity of the two-row array at different frequencies. A frequency-scanning range of 22° was achieved. Note that the cross-polarization component, emitted largely off the scanning range of the array, vanished in the complete structure (Figure 5b). Additionally, the SLL of the two-row array was higher than in the complete structure (Figure 5b) because the patterns were optimized for the prototype excited photonically. The SLL could be improved by including more periods in the row. Figure 8b shows the simulated and the measured peak gain for the two-row prototype adapted for probe measurements. The largest deviation between simulated and measured data equaled 1.4 dB, which was acceptable considering the method used to excite the antenna. This value of measured gain was also consistent with the simulated radiation efficiency (77% at broadside). In the measurements, a standard gain horn was first characterized as a reference to retrieve absolute values of gain. Additionally, the incident power upon the antenna, using the

de-embedded impedance values, was recalculated. Note the antenna did not present degraded gain at the frequency of broadside emission due to the good input matching observed in Figure 7. Therefore, the operation range was extended from the backward quadrant ($\theta < 0°$) to the broadside and the forward quadrant.

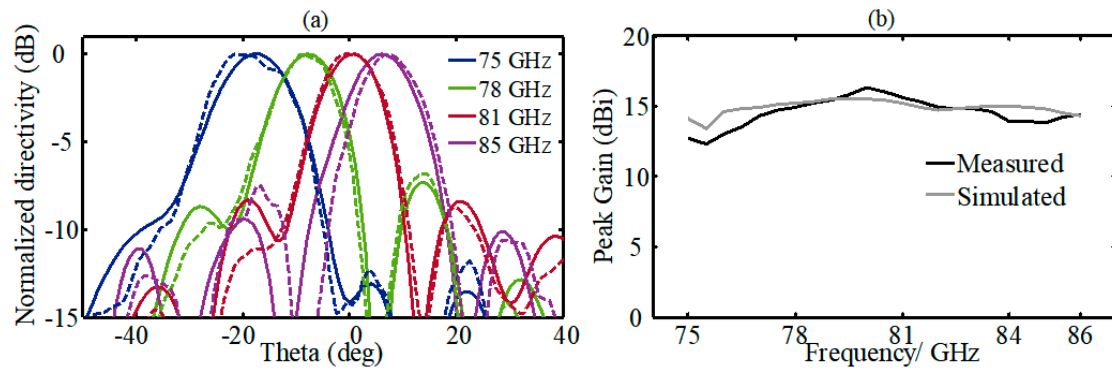**Figure 8.** (**a**) Normalized co-polar directivity at H-plane at different frequencies for the two-row prototype adapted for probe measurements. Continuous line: simulation, dashed line: measurements. (**b**) Simulated and measured peak gain.

4.2. Photonic Measurements

The antenna integrated with the UTC-PD, as described in Section 3, was used in a wireless link, as well as to measure the output power, using one active UTC-PD. The link set-up is shown in Figure 9a. A standard photonic approach [2,26] was used to generate and modulate two optical tones of two distributed feedback lasers (Toptica Photonics DFB pro BFY), with a spacing in frequency equal to that of the mm-wave carrier. After modulation using on–off keying (OOK), the signal was amplified (EDFA), monitored in an optical spectrum analyzer (OSA), and coupled to the UTC-PD input optical dielectric waveguide by a lensed fiber (OZ Optics). Subsequently, a QO system is employed to collimate the radiation. Note that the antenna radiates perpendicularly to the PCB plane (Figure 9b). Hence, it is placed at the focal point of a parabolic mirror that collimates radiation horizontally, as is most convenient for the QO link. On the receiving side, a 10 cm diameter Teflon lens focuses the radiation onto a Zero bias Schottky Barrier Diode detector (ZSBD) [27]. After the mm-wave carrier is detected, the signal, in baseband, is filtered and amplified (LNA amplifier + limiting amplifier). Finally, the detected signal is compared to the original using a BER tester (Anritsu MP2100A). The link parameters are summarized in Table 1. Figure 9c shows the corresponding eye-diagram for error-free transmission at 2.15 Gbps. At higher data-rates, variations of the antenna phase center with frequency create jitter, which in turn distorts the communication. Finally, Figure 9d shows a photograph of the assembled prototype.

Table 1. Wireless link with one active PD: summary of main parameters.

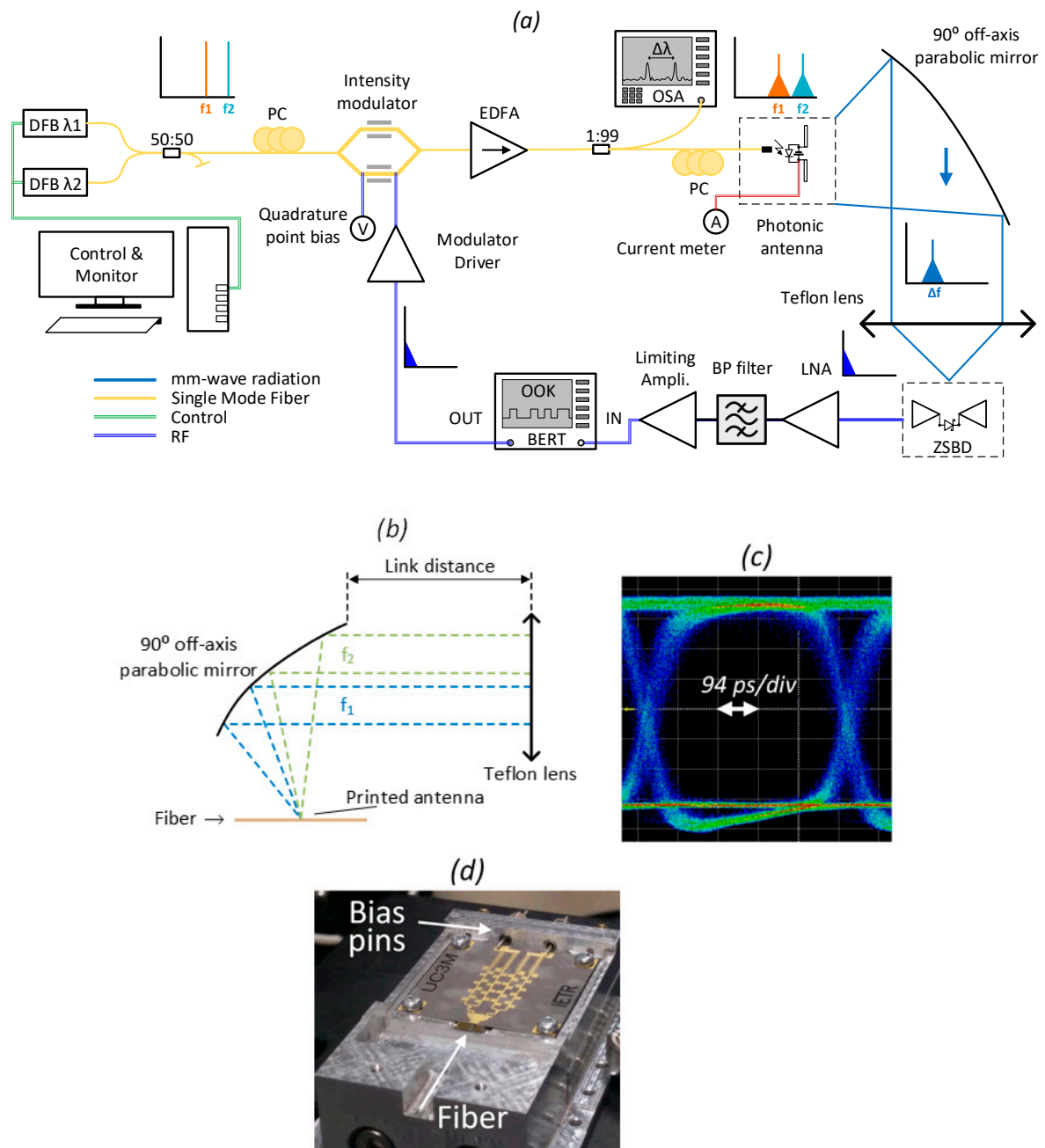| Parameter	Value
Data rate	2.15 Gbps
RF carrier	80 GHz
Modulation	OOK
Link distance	25 cm
Bit error rate	$<10^{-12}$
Photocurrent	7.0 mA

Figure 9. (**a**) Schematic of the set-up utilized for the wireless link (PC= polarization controller, BP= bandpass, LNA= low noise amplifier). (**b**) Simplified QO system, (**c**) eye diagram for the error-free transmission at 2.15 Gbps, and (**d**) photograph of the prototype.

Power measurements of the photonic prototype with a UTC-PD excited were performed on a similar set-up as the transmission link. The Teflon lens, ZSBD, and receiving chain were replaced by a THz absolute power meter (Thomas Keating Instruments). Additionally, the modulator was substituted by a fiber-coupled free-space collimator plus a chopper to enable lock-in detection. Since the broadband detector presented a large window in which pressure variations due to thermal heating were measured, external stimuli could alter measurements. Therefore, the dependence $P \propto I^2$ was checked before power measurements, P being the detected power and I the DC photocurrent. This is of utmost importance if an end-fire antenna is measured. In this case, some light, which was chopped at the same lock-in frequency, could couple and destroy the measurements. In this case, however, the previous relationship would be linear and it could be easily noted. Figure 10 shows the frequency dependence

of the detected power. It featured a 3 dB bandwidth of 11 GHz (74 GHz to 85 GHz), with a maximum of 120 μW at 80.5 GHz, for 45 mW input optical power at –2.5 V bias voltage (9.8 mA photocurrent). This was in agreement with the photodiode output power [25] when bonding losses (4–5 dB) and antenna radiation efficiency (77%) were accounted for. For frequencies out of the operation band, the mirror did not capture all the emitted radiation, emitted largely off-boresight, and the detected power decreased. This could be solved using a mirror with lower F-number or placing the power meter window horizontally, with the appropriate support and alignment structure. Nevertheless, these frequencies are not within the range of interest and are not measured in the present work.
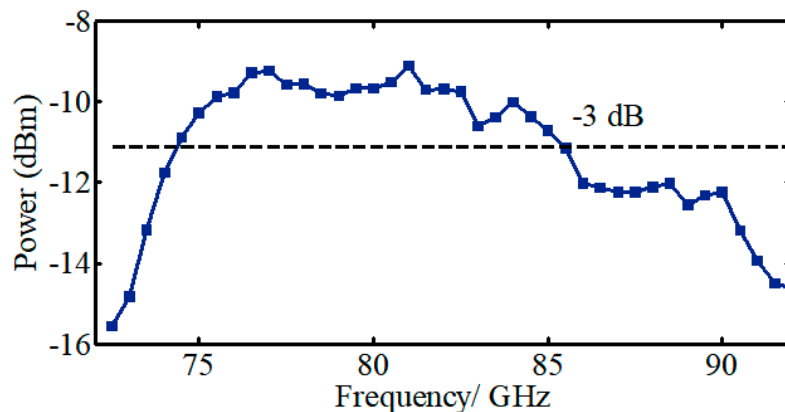

Figure 10. Detected power after the QO system.

5. Featured Application

In a potential scenario, we discuss the application of the LWA for beam alignment in wireless data center interconnections. Wireless interconnections in data centers were proposed in [28] to provide scalability and reconfigurability, which are difficult to achieve by fiber interconnected nodes as the number of servers increases. Mm-wave links at 60 GHz or sub-THz frequencies, better suited for tens of Gbps data rates, could provide a flexible alternative to an all-fiber scenario.

Figure 11a depicts a simplified data center node structure with server racks distributed in a hexagonal lattice. The servers form sub-groups that are interconnected by fiber, whereas the wireless links provide flexible interconnection between them, thus forming a hybrid architecture. More details on hybrid architectures can be found in [28].

Electronic beam steering with phased arrays is frequently proposed in the literature as a means to align the different line-of-sight (LoS) links [16,28]. However, mechanical alignment is more affordable, given the cost and energy consumption of many active elements required in a high gain phased array. As discussed next, these high-frequency data links feature high directivity and narrow beamwidth, which require dedicated hardware, as well as the corresponding protocol to control the stringent alignment.

In [18] and in the present manuscript, we reported on the LWA that produces a beam squint with frequency, which is one of the simplest forms to steer the beam. It shows a medium directivity of about 18–20 dBi, points within the 22° scan range, and works at the E-band (from 75 to 85 GHz). Owing to the antenna scalability, these characteristics can be easily adapted for a lower HPBW and enhanced pointing resolution. Indeed, the row composed of 19 periods presents an HPBW of 4° (18.5 dBi gain for one row), while maintaining good input impedance matching. Besides, the same concept can likewise be employed at other frequencies [29]. In this use case, the LWA would be co-located with the transceivers on top of the racks in a structure that would offer in-plane mechanical rotation, as shown in Figure 11b. After, the LWA could be used to establish optimum alignment between transceivers in the link. During alignment, a signal with reduced bandwidth or lock-in detection could be employed, lowering the demand for highly directive antennas and eluding a dedicated QO system. For instance,

for a detector NEP of $2\,pW/\sqrt{Hz}$ [30], and a signal bandwidth of 1 MHz, it suffices with 21 dBi directive antennas to obtain an SNR = 10 (0 dBm noiseless radiated power, 10 m distance, f = 75 GHz, and $D = G$ for the Rx antenna). For 10 GHz bandwidth, the required directivity would increase to 31 dBi.

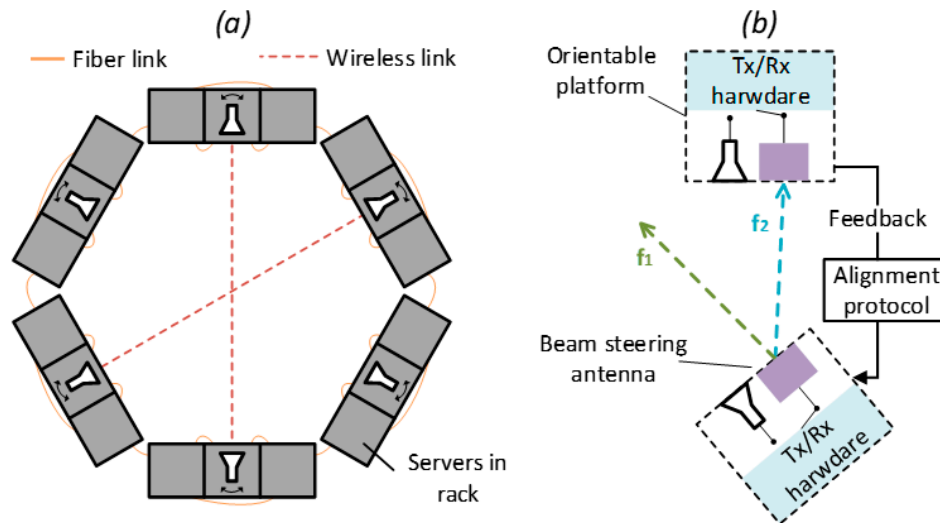**Figure 11.** (**a**) Hybrid interconnections in a data center; the continuous yellow lines represent wired fiber links whereas the dashed red lines illustrate reconfigurable wireless LoS links. (**b**) LWA set-up, co-located with the wireless transceivers, to enable alignment in a LoS link.

This solution would offer a fast and simple option for data center reconfigurability. Additionally, the transceiver hardware, represented in blue in Figure 11b, could be partially reused. For instance, it would suffice with an optical switch for a photonically generated signal to select either of the antennas. Therefore, this solution would play little role in the overall system cost or size. The PCB in which the antenna has been fabricated is 30 mm by 30 mm, with an approximate packaging footprint of around 5–10 cm^3.

6. Discussion

In this manuscript, we reported the premier work on the design, photonic integration, and characterization of a leaky-wave antenna array in PCB technology at E-band frequencies. The designed antenna exhibits beam steering with frequency and a scalable layout. Measurements of the radiation pattern are performed on a two-row array, adapted for probe excitation. A 22° scan range, including broadside, is shown across the frequency of operation of the antenna (75 GHz to 85 GHz), which is in agreement with full-wave simulations. Measurements of return losses are also in good agreement with simulations. In this respect, a method to de-embed the probe plus interconnection is described in the appendix. To the best of our knowledge, this is one of the few realizations of periodic 1-D structures in which the complete periodic structure shows adequate matching characteristics ($S_{11} < -12$ dB) at broadside. This is due to increased losses per period, which also helps to obtain a compact structure and higher radiation efficiency, and to enlarge the scanning range of the antenna from the backward quadrant to broadside and the forward quadrant. Furthermore, the antenna is tested in a wireless communications system, demonstrating error-free transmission at 2.15 Gbps and a 25 cm link distance. Finally, the application of the LWA antenna as a simple means to align mm-wave LoS links was outlined.

Author Contributions: Conceptualization, Á.J.P.-G., R.S., L.E.G.-M., and D.G.-O.; methodology, Á.J.P.-G., M.A., and G.C.D.B.; formal analysis, Á.J.P.-G.; investigation, Á.J.P.-G., M.A., G.C.D.B., L.B., and F.F.; writing—original draft preparation, Á.J.P.-G.; writing—review and editing, L.E.G.-M., R.S., and D.G.-O.; supervision, G.C.D.B., R.S., L.E.G.-M., and D.G.-O.; funding acquisition, G.C.D.B., R.S., L.E.G.-M., and D.G.-O. All authors have read and agreed to the published version of the manuscript.

Appendix A. Method for Probe De-Embedding

S-parameter measurements at mm-wave frequencies with coplanar probes comprise the challenge of probe and interconnection de-embedding. Indeed, the ground signal ground (GSG) probe interconnection with the device under test (DUT), as well as the probe itself, can introduce a relevant contribution to the overall measurement, and thus its effect has to be removed for an accurate determination of *S*-parameters. Besides, for one-port components, only one-port probe measurements might be available. In this section, we describe the procedure employed to de-embed the probe and the interconnection from S_{11} measurements.

The difficulty of fabrication of 50-Ω loads at mm-wave frequencies in the same substrate as the DUT makes the use of the standard short-open-load-through (SOLT) calibration impractical [31]. Another of the standard methods, through-reflection-line (TRL), requires the use of two probes. Finally, one finds open-short (OS) or the short-open (SO) methods, which include the modeling of parasitic lumped elements introduced by the probes plus interconnection. These methods, however, rely on a specific probe plus interconnection, and it was shown in [31] that beyond 30 GHz substantial discrepancies existed between both for a reverse-biased Schottky diode on a silicon substrate.

The method presented herein is a variant from [31] based on simulation plus measurements. Instead of imposing $S_{11} = S_{22}$, as it is done in [31], an additional load is measured to obtain a fourth relation. It consists of a set of four measurements, three on test loads whose values are assumed, plus another one on the DUT. The three measurements plus the reciprocity condition yield four relations from which the ABCD parameters of the interconnection can be retrieved analytically. It is also assumed that its ABCD matrix is maintained through measurements. This implies that the same interconnect has to be used, in addition to landing the probes at the same positions. The measurement schematic is shown in Appendix A Figure A1.

The S_{11} parameter at a calibrated reference plane of an arbitrary structure plus load, Z_L, is given by Equation (A1), where A, B, C, and D are the ABCD-matrix elements of the structure between the load and the reference plane:

$$S_{11} = -\frac{Z_c Z_L C + Z_c D - A Z_L - B}{Z_c Z_L C + Z_c D + A Z_L + B} \tag{A1}$$

A short-circuit (S) and an open circuit (O) are loads that can be relatively simply manufactured in the same conditions as the DUT. Substituting in Equation (A1), the corresponding relations are found for S and O:

$$D = \frac{B\left(1 - S_{11}^S\right)}{Z_c\left(1 + S_{11}^S\right)}, \tag{A2}$$

$$C = \frac{A\left(1 - S_{11}^o\right)}{Z_c\left(1 + S_{11}^o\right)}. \tag{A3}$$
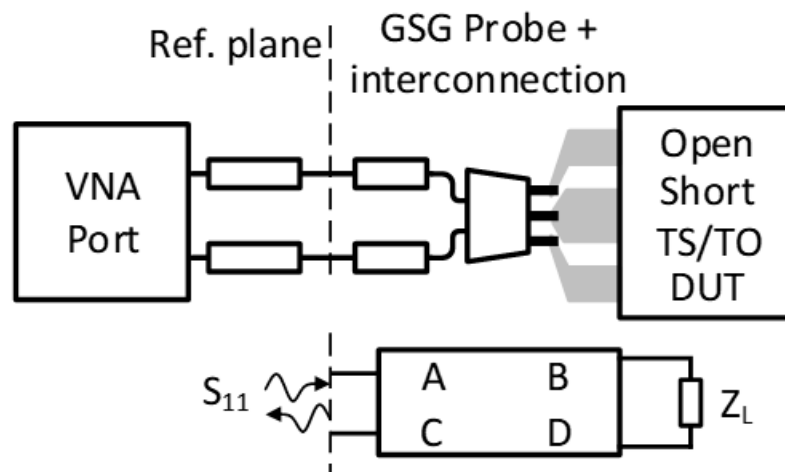
Figure A1. Schematic used for 1-port S_{11} measurements with different loads: open, short, translated short (TS), translated open (TO), and device under test (DUT), as well as the corresponding network equivalent.

If the probe plus interconnect structure are composed of passive, isotropic materials, one can enforce reciprocity and obtain the following relation:

$$AD - BC = 1 \qquad (A4)$$

Finally, a third load is measured to obtain from Equation (A1) the fourth relation. It consists of a translated short (TS) or translated open (TO). The surge impedance of the transmission line, Zc, and the propagation constant, are obtained from full-wave simulations. These are parameters that can be easily simulated for standard low-loss 50-Ω transmission lines. The translated length of the load is chosen as λ/8 to distribute evenly the three loads on the Smith chart. Note that if broadband measurements are performed, different windows of frequencies will require different translated lengths.

The manufactured O, S, and TS are shown in Appendix A Figure A2a–c, as well as one DUT (two-row array) in Figure A2d. To minimize the effect of the GSG pads, and to adapt the probe pitch to the G-CPW, a tapered interconnection is optimized (Appendix A Figure A2e). Additionally, the short and open structures are optimized using full-wave simulations to obtain nominal S_{11} parameters. The same interconnect geometry is used among devices and also redundant samples are measured to ensure that assuming the ABCD matrix constant is a valid supposition.
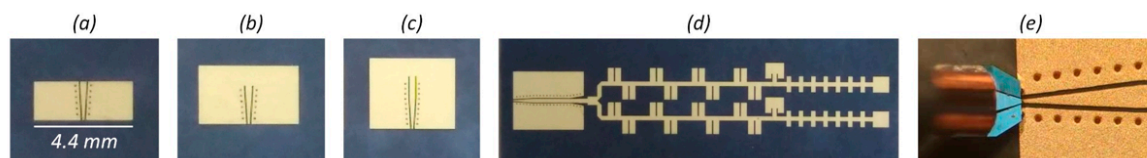

Figure A2. Different structures measured for probe de-embedding in *S*-parameter measurements: (**a**) open-circuit, (**b**) short-circuit, (**c**) translated short, and (**d**) DUT. In this example it consist of a two-row stub array. (**e**) Detail of the probe tip and tapered interconnection shared among structures.

References

1. Preu, S.; Döhler, G.H.; Malzer, S.; Stöhr, A.; Rymanov, V.; Göbel, T.; Brown, E.R.; Feiginov, M.; Gonzalo, R.; Beruete, M.; et al. Principles of THz generation. In *Semiconductor Terahertz Technology: Devices and Systems at Room Temperature Operation*, 1st ed.; Carpintero, G., García-Muñoz, L.E., Hartnagel, H.L., Preu, S., Räisänen, A.V., Eds.; John Wiley & Sons, Inc.: Hoboken, NJ, USA, 2015.

2. Nagatsuma, T.; Hisatake, S.; Fujita, M.; Pham, H.H.N.; Tsuruda, K.; Kuwano, S.; Terada, J. Millimeter-wave and terahertz-wave applications enabled by photonics. *IEEE J. Quantum Electron.* **2016**, *52*, 1–12. [CrossRef]

3. Ali, M.; Jankowski, A.; Guzman, R.C.; García-Muñoz, L.E.; van Dijk, F.; Carpintero, G. Photonics-based compact broadband transmitter module for E-band wireless communications. In Proceedings of the 2019 49th European Microwave Conference (EuMC), Paris, France, 1–3 October 2019; IEEE: Paris, France, 2019; pp. 808–811.

4. Koenig, S.; Lopez-Diaz, D.; Antes, J.; Boes, F.; Henneberger, R.; Leuther, A.; Tessmann, A.; Schmogrow, R.; Hillerkuss, D.; Palmer, R.; et al. Wireless sub-THz communication system with high data rate. *Nat. Photonics* **2013**, *7*, 977–981. [CrossRef]

5. Nagatsuma, T.; Carpintero, G. Recent progress and future prospect of photonics-enabled Terahertz communications research. *IEICE Trans. Electron.* **2015**, *98*, 1060–1070. [CrossRef]

6. Hirata, A.; Ishii, H.; Nagatsuma, T. Design and characterization of a 120-GHz millimeter-wave antenna for integrated photonic transmitters. *IEEE Trans. Microw. Theory Tech.* **2001**, *49*, 2157–2162. [CrossRef]

7. Li, X.; Yu, J. Over 100 Gb/s ultrabroadband MIMO wireless signal delivery system at the D-band. *IEEE Photonics J.* **2016**, *8*, 1–10. [CrossRef]

8. Nagatsuma, T.; Oogimoto, K.; Yasuda, Y.; Fujita, Y.; Inubushi, Y.; Hisatake, S.; Agoues, A.M.; Lopez, G.C. 300-GHz-band wireless transmission at 50 Gbit/s over 100 meters. In Proceedings of the 2016 41st International Conference on Infrared, Millimeter, and Terahertz waves (IRMMW-THz), Copenhagen, Denmark, 25–30 September 2016; IEEE: Copenhagen, Denmark, 2016; pp. 1–2.

9. Hirata, A.; Kosugi, T.; Meisl, N.; Shibata, T.; Nagatsuma, T. High-Directivity photonic emitter using photodiode module integrated with HEMT amplifier for 10-Gbit/s wireless link. *IEEE Trans. Microw. Theory Technol.* **2004**, *52*, 1843–1850. [CrossRef]

10. Peytavit, E.; Beck, A.; Akalin, T.; Lampin, J.-F.; Hindle, F.; Yang, C.; Mouret, G. Continuous terahertz-wave generation using a monolithically integrated horn antenna. *Appl. Phys. Lett.* **2008**, *93*, 111108. [CrossRef]

11. Rey, S.; Merkle, T.; Tessmann, A.; Kürner, T. A phased array antenna with horn elements for 300 GHz communications. In Proceedings of the 2016 International Symposium on Antennas and Propagation (ISAP), Okinawa, Japan, 24–28 October 2016; IEEE: Okinawa, Japan, 2016; pp. 122–123.

12. Bauerschmidt, S.T.; Döhler, G.H.; Lu, H.; Gossard, A.C.; Malzer, S.; Preu, S. Arrayed free space continuous-wave terahertz photomixers. *Opt. Lett.* **2013**, *38*, 3673–3676. [CrossRef] [PubMed]

13. Preu, S.; Muller-Landau, C.; Malzer, S.; Döhler, G.H.; Lu, H.; Gossard, A.C.; Segovia-Vargas, D.; Rivera-Lavado, A.; Garcia-Munoz, L.E. Fiber-Coupled 2-D n-i-pn-i-p superlattice photomixer array. *IEEE Trans. Antennas Propag.* **2017**, *65*, 3474–3480. [CrossRef]

14. Shimizu, N.; Nagatsuma, T. Photodiode-integrated microstrip antenna array for subterahertz radiation. *IEEE Photonics Technol. Lett.* **2006**, *18*, 743–745. [CrossRef]

15. Kalimulin, R.; Artemenko, A.; Maslennikov, R.; Putkonen, J.; Salmelin, J. Impact of mounting structures twists and sways on point-to-point millimeter-wave backhaul links. In Proceedings of the 2015 IEEE International Conference on Communication Workshop (ICCW), London, UK, 8–12 June 2015; IEEE: London, UK, 2015; pp. 19–24.

16. Katayama, Y.; Takano, K.; Kohda, Y.; Ohba, N.; Nakano, D. Wireless data center networking with steered-beam mmWave links. In Proceedings of the 2011 IEEE Wireless Communications and Networking Conference, Cancun, Mexico, 28–31 March 2011; IEEE: Cancun, Mexico, 2011; pp. 2179–2184.

17. Rupakula, B.; Nafe, A.; Zihir, S.; Wang, Y.; Lin, T.W.; Rebeiz, G. 63.5–65.5-GHz transmit/receive phased-array communication link with 0.5–2 Gb/s at 100–800 m and ± 50° scan angles. *IEEE Trans. Microw. Theory Technol.* **2018**, *66*, 4108–4120. [CrossRef]

18. Pascual, A.J.; Ali, M.; García-Muñoz, L.E.; Carpintero, G.; van Dijk, F.; González-Ovejero, D.; Sauleau, R. A scalable photomixing array for increased emitted power. In Proceedings of the 2019 44th International Conference on Infrared, Millimeter, and Terahertz Waves (IRMMW-THz), Paris, France, 1–6 September 2019; IEEE: Paris, France, 2019; pp. 1–2.

19. Jackson, D.R.; Oliner, A.A. Leaky-wave antennas. In *Modern Antenna Handbook*, 1st ed.; Balanis, C.A., Ed.; John Wiley & Sons, Inc.: Hoboken, NJ, USA, 2008.

20. Lafond, O.; Himdi, M. Printed Millimeter Antennas– Multilayer Technologies. In *Advanced Millimeter-Wave Technologies*, 1st ed.; Liu, D., Gaucher, B., Pfeiffer, U., Grzyb, J., Eds.; John Wiley & Sons, Ltd.: Chichester, UK, 2009.

21. James, J.R.; Hall, P.S.; Wood, C. Radiation mechanism of an open-circuit microstrip termination. In *Microstrip Antenna: Theory and Design*, 1st ed.; Peter Peregrinus Ltd.: London, UK, 2015.

22. James, J.R.; Hall, P.S. Microstrip antennas and arrays. Part 2: New array-design technique. *IEE J. Microw. Opt. Acoust.* **1977**, *1*, 175–181. [CrossRef]

23. Paulotto, S.; Baccarelli, P.; Frezza, F.; Jackson, D.R. A novel technique for open-stopband suppression in 1-D periodic printed leaky-wave antennas. *IEEE Trans. Antennas Propag.* **2009**, *57*, 1894–1906. [CrossRef]

24. Hirata, A.; Minotani, T.; Ito, H.; Hirota, Y.; Ishibashi, T.; Sasaki, A.; Nagatsuma, T. High-power photonic millimetre wave generation at 100 GHz using matching-circuit-integrated uni-travelling-carrier photodiodes. *IEE Proc. Optoelectron.* **2003**, *150*, 138–142.

25. Rouvalis, E.; Chtioui, M.; Tran, M.; Lelarge, F.; van Dijk, F.; Fice, M.J.; Renaud, C.C.; Carpintero, G.; Seeds, A.J. High-speed photodiodes for InP-based photonic integrated circuits. *Opt. Express* **2012**, *20*, 9172–9177. [CrossRef] [PubMed]

26. García-Muñoz, E.; Abdalmalak, K.A.; Santamaría, G.; Rivera-Lavado, A.; Segovia-Vargas, D.; Castillo-Araníbar, P.; van Dijk, F.; Nagatsuma, T.; Brown, E.R.; Guzman, R.C.; et al. Photonic-based integrated sources and antenna arrays for broadband wireless links in terahertz communications. *Semicond. Sci. Technol.* **2019**, *34*, 054001. [CrossRef]

27. Ali, M.; Guzman, R.C.; Rivera-Lavado, A.; Cojocari, O.; García-Muñoz, L.E.; Carpintero, G. Quasi-optical schottky barrier diode detector for mmWave/sub-THz wireless communication. In Proceedings of the 2018 25th International Conference on Telecommunications (ICT), St. Malo, France, 26–28 June 2018; IEEE: St. Malo, France, 2018; pp. 279–282.

28. Vardhan, H.; Thomas, N.; Ryu, S.-R.; Banerjee, B.; Prakash, R. Wireless data center with millimeter wave network. In Proceedings of the 2010 IEEE Global Telecommunications Conference GLOBECOM 2010, Miami, FL, USA, 6–10 December 2010; IEEE: Miami, FL, USA, 2010; pp. 1–6.

29. Mahmoud, A.; Gonzalez-Ovejero, D.; Ettorre, M.; Sauleau, R.; Aniel, F.; Zerounian, N.; Grimault-Jacquin, A.-S. High gain constrained lens antenna on BCB substrate for 300-GHz applications. In Proceedings of the 2019 IEEE International Symposium on Antennas and Propagation and USNC-URSI Radio Science Meeting, Atlanta, GA, USA, USA, 7–12 July 2019; IEEE: Atlanta, GA, USA, 2019; pp. 507–508.

30. Hesler, J.L.; Crowe, T.W. NEP and responsivity of THz zero-bias Schottky diode detectors. In Proceedings of the 2007 Joint 32nd International Conference on Infrared and Millimeter Waves and the 15th International Conference on Terahertz Electronics, Cardiff, UK, 2–9 September 2007; IEEE: Cardiff, UK, 2007; pp. 844–845.

31. Xu, H.; Kasper, E. A de-embedding procedure for one-port active mm-wave devices. In Proceedings of the 2010 Topical Meeting on Silicon Monolithic Integrated Circuits in RF Systems (SiRF), New Orleans, LA, USA, 11–13 January 2010; IEEE: New Orleans, LA, USA, 2010; pp. 37–40.